Biosensors and Bioelectronics 145 (2019) 111711

Contents lists available at ScienceDirect

Biosensors and Bioelectronics

journal homepage: www.elsevier.com/locate/bios

Ultraselective antibiotic sensing with complementary strand DNA assisted aptamer/MoS_2 field-effect transistors

Xiaoyan Chen[a,b], Sibei Hao[a,b], Boyang Zong[a,b], Chengbin Liu[a,b], Shun Mao[a,b,*]

[a] Biomedical Multidisciplinary Innovation Research Institute, Shanghai East Hospital, State Key Laboratory of Pollution Control and Resource Reuse, College of Environmental Science and Engineering, Tongji University, 1239 Siping Road, Shanghai 200092, China
[b] Shanghai Institute of Pollution Control and Ecological Security, Shanghai 200092, China

ARTICLE INFO

Keywords:
Antibiotic sensing
Field-effect transistor
MoS_2 nanosheet
Aptamer
Complementary strand DNA

ABSTRACT:

Although aptamer has been demonstrated as an important probe for antibiotic determination, the selective sensing of different antibiotics is still a challenge due to their structure similarities and wide folding degrees of aptamer. Herein, a field-effect transistor using MoS_2 nanosheet as the channel and an aptamer DNA (APT) with its configuration shaped by a complementary strand DNA (CS) is employed for kanamycin (KAN) determination. This probe structure contributes to an enhanced selectivity and reliability with reduced device-to-device variations. This MoS_2/APT/CS sensor shows time-dependent performance in antibiotic sensing. Prolonged detection time (20 s–300 s) leads to an enhanced sensitivity (1.85–4.43 M^{-1}) and a lower limit of detection (1.06–0.66 nM), while a shorter detection time leads to a broader linear working range. A new sensing mechanism relying on charge release from probe is proposed, which is based on the "replacement reaction" between KAN and APT-CS. This sensor exhibits an extremely high selectivity (selectivity coefficient of 12.8) to kanamycin over other antibiotics including streptomycin, tobramycin, amoxicillin, ciprofloxacin and chloramphenicol. This work demonstrates the merits of probe engineering in label-free antibiotic detection with FET sensor, which presents significant promises in sensitive and selective chemical and biological sensing.

1. Introduction

Antibiotic residues are emerging water pollutants, which pose serious ecological and health risks (Boxall et al., 2012). The increasing concern on long-term impact of antibiotic on environmental ecology and public safety leads to a growing demand for advanced sensing technologies to monitor their level in environmental media. Traditional techniques for antibiotic detections are based on chromatography-related methods (Bayen et al., 2014; Tlili et al., 2016; Turiel et al., 2003), microbiological assay (Knecht et al., 2004), and enzyme-linked immunosorbent assay (ELISA) (Kumar et al., 2004). Chromatography-based methods normally have high-cost and are time-consuming due to complicated pre-treatment and post-processing with a lack of portability, while microbiological assay has difficulties in achieving repeatable analysis and accurate quantification. Though ELISA has been widely used as a commercial method, it also suffers from the enzyme inactivation as well as long detecting time. These methods are not suitable for *in-situ* or real-time antibiotic monitoring. To meet the demand for *in-situ* and real-time monitoring of antibiotics in water for early warming and prompt treatment, sensing strategies and devices that are capable for real-time and *in-situ* detection become a research focus (Fang et al., 2019; Wang et al., 2017a).

Field-effect transistor (FET) sensors recently have received much attention due to their high sensitivity and short sensing time (Fu et al., 2017; Knopfmacher et al., 2014; Li et al., 2019; Zhang et al., 2015). Considering the miniaturized and integratable configuration, FET sensors also show potential as portable sensing devices to realize real-time and *in-situ* monitoring of water contaminants. As discussed in our recent review article, two-dimensional (2D) nanomaterials including graphene, transitional metal dichalcogenides (TMDs) and phosphorene (BP), become promising choices as the channel material in FET sensors. It is attributed to their fascinating structures (*i.e.*, high specific surface area and nanosheet morphology) and electronic properties (*i.e.*, high carrier mobility) (Fu et al., 2017; Mao et al., 2017; Vicarelli et al., 2012). Graphene is one of the most studied 2D nanomaterials in FET sensors. However, the semimetal property (zero bandgap) and low on-off ratio in graphene FET limit its sensing application (Meric et al., 2008). As an emerging 2D material, BP has been reported in FET

* Corresponding author. Biomedical Multidisciplinary Innovation Research Institute, Shanghai East Hospital, State Key Laboratory of Pollution Control and Resource Reuse, College of Environmental Science and Engineering, Tongji University, 1239 Siping Road, Shanghai 200092, China.
E-mail address: shunmao@tongji.edu.cn (S. Mao).

https://doi.org/10.1016/j.bios.2019.111711
Received 19 May 2019; Received in revised form 25 August 2019; Accepted 16 September 2019
Available online 19 September 2019
0956-5663/

sensors; however, the poor chemical stability and durability in ambient condition become a key challenge for its real application (Island et al., 2015). 2D molybdenum disulfide (MoS_2), a typical TMD, has attracted increasing research interest as an ideal choice in FET devices due to its competitive electronic properties with sufficient stability. Single- and few-layer MoS_2 is a semiconductor with a direct bandgap (~1.8 eV), which can be tuned by the number of atomic layers (Wang et al., 2012). The layer-dependent semiconducting properties, high on-off ratio (~10^8) and carrier mobility (60 $cm^2V^{-1}s^{-1}$ at 250 K) of MoS_2 suggests a significant potential of MoS_2 FET for biological and chemical sensing (Fuhrer and Hone, 2013; Radisavljevic et al., 2011; Radisavljevic and Kis, 2013). In past few years, MoS_2-based FET sensors have been reported for heavy metal (Zhou et al., 2016), protein (Wang et al., 2014), and biomarker detection (Majd et al., 2018). However, antibiotic sensing with MoS_2-based FET sensors has not yet been reported.

Selective sensing is the main focus and a bottleneck in antibiotic sensor development, which greatly limits the real application of sensing platforms. For FET sensor, generally, the selective sensing of antibiotic relies on the sensing probe, which can specifically bind or interact with target antibiotic molecule. Since antibiotics are structurally complex, bio-recognition with antigen-antibody interaction or enzyme could be a choice; however, these probes have limitations in their stability and easy to be influenced by foreign substances in working media. As an emerging bio-recognition element, aptamer is an artificial single strand DNA (ssDNA) or RNA obtained by systematic evolution of ligands by exponential enrichment (SELEX), which has superiorities in specificity, stability and low-cost (Darmostuk et al., 2015). It is potential to achieve highly selective antibiotic sensing with an enhanced chemical stability with aptamer probe. Moreover, the hydrolysis of phosphodiester bond on nucleotide leads to the negatively charged nature of aptamer in water. Based on this, aptamer has been proved overcoming limitations of Debye screening effect on FET water sensors and has been demonstrated in aptamer/graphene FET sensor (Chen et al., 2019; Nakatsuka et al., 2018). Although few studies about antibiotic detection using aptamer/graphene FETs were reported, the application of aptamer potentially opened a new era for MoS_2-based FET sensing platform (Chen et al., 2019; Wang et al., 2016).

In this study, we report the first MoS_2-based FET sensor for label-free detection of antibiotics. The target antibiotic is kanamycin (KAN), a commonly used aminoglycoside with a narrow safety margin. In this sensor, atomically thin MoS_2 obtained from liquid-phase intercalation and exfoliation was used as the channel material in FET platform. To ensure a selective detection, in our design, a new probe geometry was constructed. The aptamer DNA (APT) for kanamycin is modified on MoS_2 surface via gold nanoparticles (AuNPs) as the linker, and folds into a conjugate structure with the help of short complementary strand DNA (CS). The base sequences along CS are complementary to both ends of the aptamer, attaching on the APT through base pairing. Superior to single strand aptamer as the probe, this new probe geometry enables enhanced sensing reliability and selectively. On one hand, long single strand aptamer DNA has high degree of freedom and each of the probe exhibits different levels of folding due to physical bending and intrachain base pairing. With CS, a much shorter strand that pairs with the long APT chain, the APT is shaped into a short and accordant structure, and the configurational diversity of each single probe is reduced. Thus, the APT/CS conjugate helps to reduce the device-to-device variations. On the other hand, a new sensing mechanism of MoS_2 FET sensor is proposed based on the release of charges from probe through a “replacement reaction”, different from the reported sensing strategy relying on a direct aptamer-antibiotic binding, which lacks selectivity (especially among antibiotics in the same category). Since this replacement reaction only occurs when there is a stronger binding than APT-CS base pairing, those influences from nonspecific antibiotics and structural analogs can be greatly minimized, improving the sensing specificity (Wang et al., 2016; Zhao et al., 2015).

This MoS_2/APT/CS sensor shows a quick response to KAN with a limit of detection (LOD) on nM level. Due to the replacement reaction, this sensor shows time-dependent performance in KAN sensing. Prolonged detection time leads to an enhanced sensitivity and a lower LOD, while a shorter detection time leads to a broader concentration sensing range. More importantly, the sensor shows ultra-selective performance in KAN detection against other antibiotics of four categories. The selectivity coefficient (defined as the ratio of the response of target analyte to that of interfering chemicals) of our sensor is up to 12.8, much higher than most of the reported KAN sensing platforms (Table S1, Supporting Information). It is believed that this new probe design strategy will help and promote future development of highly sensitive and selective FET sensing platform for *in-situ* and real-time monitoring of chemicals and biomolecules.

2. Experimental

2.1. Materials

The MoS_2 powder was purchased from XFNANO Co., Ltd. (Nanjing, China). 2D MoS_2 dispersion was obtained by lithium-based liquid-phase intercalation and exfoliation method (Wang et al., 2012). The thiol modified aptamer DNA for kanamycin (APT, thiol-5′-TGG GGG TTG AGG CTA AGC CGA-3′) and its complementary strand (CS, 5′-TCG GCT CCC CCA-3′) were prepared by SELEX technique and purified by HPLC in Sangon Biotech Co., Ltd. (Shanghai, China). APT was dispersed in bond-breaker TCEP solution at a concentration of 100 μM before use. Diphenylamine indicator was prepared by 15 g/L diphenylamine in acetic acid with 1.5% sulfuric acid and 0.2% acetaldehyde. Antibiotics (kanamycin, tobramycin, amoxicillin, chloramphenicol, and ciprofloxacin) and chemical reagents were purchased from Aladdin Chemical Reagent Co., Ltd. (Shanghai, China), used as received. The antibiotic molecular formulas are presented in Fig. S1. All the antibiotic samples were dispersed in 0.1 mM PBS buffer and aqueous solutions were prepared with DI water (18.4 MΩ) from Milli-Q Ultra-pure water system.

2.2. Sensor fabrication

Optical lithography was used to fabricate interdigitated gold electrode (50 nm thick) on Si/SiO_2 substrate (highly doped silicon wafer with a 300 nm-thick oxide layer). The finger-width and inter-finger spacing of gold electrodes are 2 μm and 1.5 μm, respectively. To deposit MoS_2 nanosheet, one drop of 0.05 mg/mL MoS_2 aqueous dispersion was pipetted onto the finger area and was rapidly dried under heat lamp. To functionalize the sensing probe, gold nanoparticles (AuNPs) were deposited onto MoS_2 using Leica EM ACE 200 sputter coater before being incubated with APT or APT/CS for 12 h. APT/CS and APT were modified on MoS_2/Au through Au–S bond. The device fabrication procedure is illustrated in Fig. S2.

2.3. Characterizations

Hitachi 4800 UHR FE scanning electron microscope (SEM), JEOL 2100F field-emission high-resolution transmission electron microscope (TEM/HRTEM), and NT-MDT Prima atomic force microscope (AFM, contacted mode) were used to characterize the morphology of MoS_2 nanosheet before and after DNA modification. Raman spectra was carried out on HORIBA HR Evolution Raman spectrometer with 532 nm laser excitation.

2.4. Sensing tests

A Keithley 4200-SCS semiconductor system was employed to analyze the electronic properties and sensing performance of FET sensors. The output characteristics were obtained by recording source-drain current (I_{ds}) while sweeping source-drain voltage (V_{ds}) (from −1.0 V to +1.0 V, step = +0.02 V). The transfer characteristics were given by

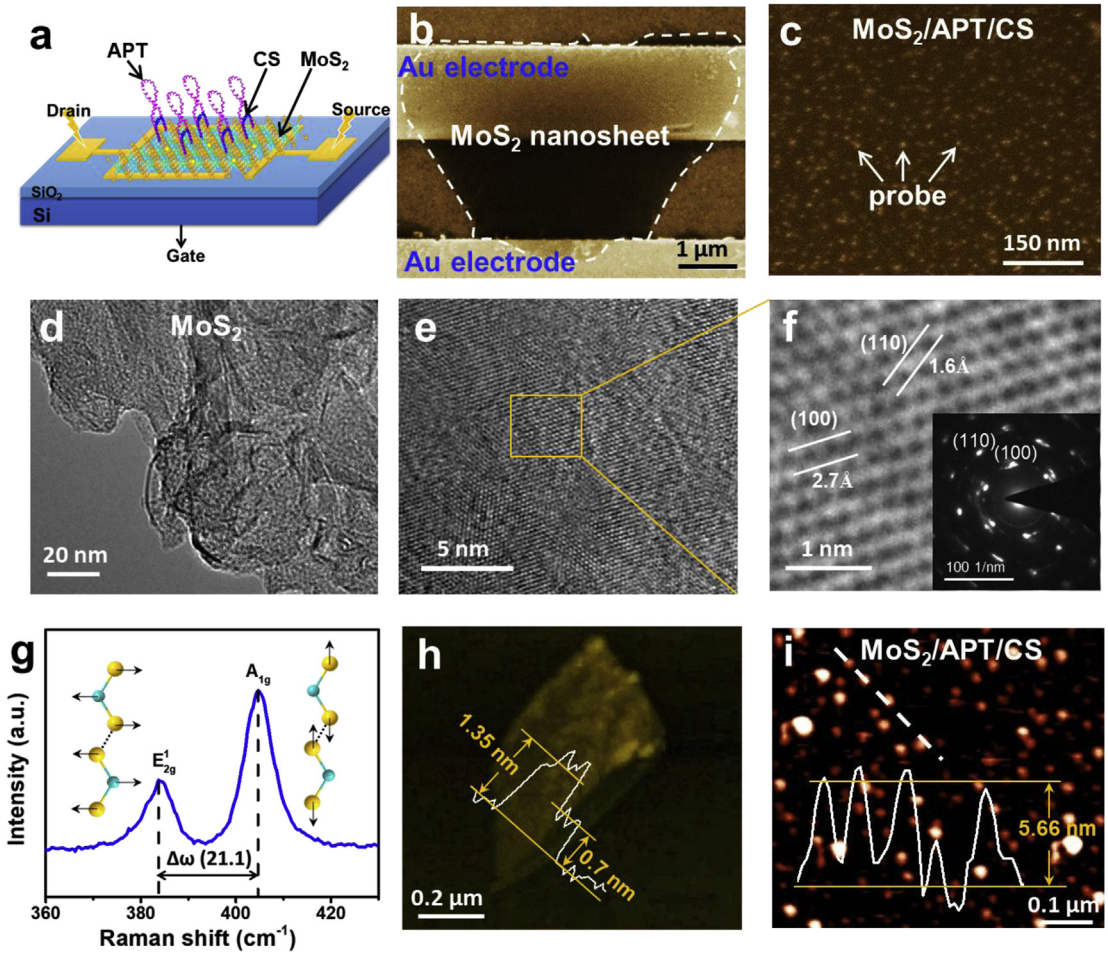

Fig. 1. (a) Schematic diagram of MoS2/APT/CS sensing platform. SEM images of (b) MoS2 nanosheet bridging adjacent finger electrodes and (c) MoS2/APT/CS hybrid at higher magnification. (d) TEM and (e–f) HRTEM images of MoS2 nanosheets. The inset (f) is the selected-area electron diffraction (SAED) patterns of MoS2 nanosheet. (g) Raman spectrum of MoS2 nanosheet shows 21.1 cm-1 frequency difference between E2g and A1g modes. AFM images of (h) MoS2 nanosheet and (i) MoS2/APT/CS hybrid. The height profiles respectively trace along the bottom yellow line and white dotted line. (For interpretation of the references to color in this figure legend, the reader is referred to the Web version of this article.)

measuring I_{ds} as a function of gate voltage (V_g) (from −40 V to +40 V, step = +0.05 V). Sensing tests were carried out by recording the real-time source-drain current when adding sample solutions with varying antibiotic concentrations onto sensing area. Specifically, the source-drain voltage is set at +0.1 V and the gate is grounded in sensing tests.

3. Results and discussion

3.1. Structure and electrical properties of MoS_2 FET

The structure of MoS_2/APT/CS sensing platform is schematically shown in Fig. 1a. The sensor device was fabricated by a layer-by-layer process, in which MoS_2 nanosheet was first deposited within finger electrode area as channel material, then aptamer DNA was functionalized onto MoS_2 surface through AuNPs and paired with complementary strands (CS). Fig. 1b shows an SEM image of an individual MoS_2 nanosheet bridging adjacent two electrodes. Fig. 1c shows higher magnification SEM image of a MoS_2 nanosheet functionalized with AuNPs/APT/CS hybrids. It is found that AuNPs are uniformly distributed on the surface of MoS_2 nanosheet. Since MoS_2 shows layer dependent semiconducting property, the laminated structure of MoS_2 was further characterized. TEM image of MoS_2 nanosheet in Fig. 1d displays a laminar structure and HRTEM image in Fig. 1e shows a honeycomb crystalline structure of MoS_2, in which bright dots indicate molybdenum and sulfur atoms. The hexagonal crystalline structure of MoS_2 was also confirmed by selected-area electron diffraction (SAED) patterns. The spacing of ~2.7 Å for (100) crystal plane and ~1.6 Å for (110) crystal plane of MoS_2 are shown in Fig. 1f, corresponding to lattice parameters of 2H–MoS_2. The slight tails in SAED pattern are due to another single Mo–S–Mo layer at angles to the tested surface.

Raman spectroscopy was also used to study the layer structure of MoS_2. The peak frequency shift ($\Delta\omega$) of E^1_{2g} and A_{1g} modes is thickness-dependent, in which E^1_{2g} and A_{1g} modes reflect the in-plane and inter-layer vibrations of MoS_2, respectively (Lee et al., 2010). As shown in Fig. 1g. MoS_2 nanosheet shows two modes at 383.6 cm^{-1} (E^1_{2g}) and 404.7 cm^{-1} (A_{1g}), respectively, with a $\Delta\omega$ of 21.1 cm^{-1}. This $\Delta\omega$ number is between the level of monolayer (19 cm^{-1}) and bilayer (22.2 cm^{-1}), indicating that the channel MoS_2 nanosheet has one to two layers. The layer structure and thickness of MoS_2 nanosheet were investigated by AFM measurements (Fig. 1h). The 2D AFM image and height profile along a folded MoS_2 nanosheet shows that the MoS_2 nanosheet has 1–2 layers (single-layer MoS_2 is ~0.7 nm thick) (Radisavljevic et al., 2011). The MoS_2 nanosheet functionalized with AuNPs/APT/CS was also studied and the surface roughness given by AFM image in Fig. 1i shows an average probe height of ~5.66 nm. The AFM results confirm the probe functionalization on MoS_2 nanosheet, and the height profile is useful to understand the KAN sensing mechanism in later discussion.

Output and transfer characteristics of FET device are fundamentals for its sensing performance. In this study, electrical characteristics of

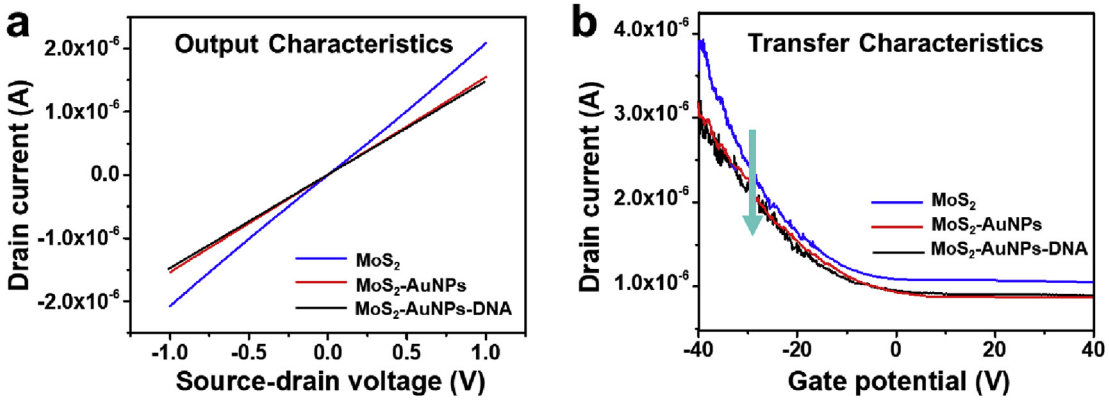

Fig. 2. (a) Output characteristics (I–V curves) before and after AuNPs deposition and probe modification on MoS2. Parameters: Vds = −1.0 to +1.0 V, step = 0.02 V; Vgs = 0 V. (b) Transfer characteristics before and after AuNPs deposition and probe modification on MoS2. Parameters: Vds = +0.1 V, Vgs = −40 to +40 V, step = 0.05 V.

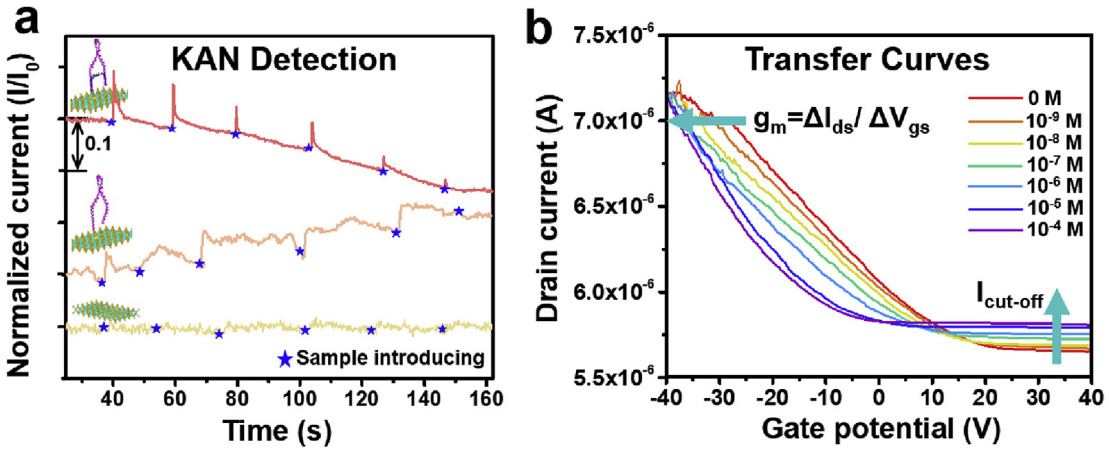

Fig. 3. (a) Real-time current responses of KAN with MoS2, MoS2/APT and MoS2/APT/CS platforms. Normalized current is obtained from I/I0, in which I is the current signal and I0 is the initial device current before sensing. Sample addition time is marked with asterisk. (b) Transfer curves of MoS2/APT/CS platform with KAN concentrations of 0 M, 10-9 M, 10-8 M, 10-7 M, 10-6 M, 10-5 M and 10-4 M.

MoS_2 FET in each modification process were investigated. I–V curves were measured to demonstrate the output characteristic of MoS_2 FET. As shown in Fig. 2a, the linear I_{ds}-V_{ds} curves for in each MoS_2 modification process demonstrate a good Ohmic contact between gold electrodes and MoS_2 nanosheet. In principle, electron transfer from a phase with higher work function to the lower can equalize Fermi levels between metal-semiconductor contact. The transference of electron from gold electrode (5.1 eV) to MoS_2 nanosheet (4.2 eV) results in space electric field perpendicular to MoS_2 surface, pointing from body to surface and thus the band bends upwards. Different from Schottky contact, since MoS_2 is p-type semiconductor as shown in Fig. 2b, this electric field leads to a high density of majority carriers (holes) within the reverse barrier layer, contributing to charge transfer, thus showing Ohmic contact (Chuang et al., 2016; Min et al., 2016; Wang et al., 2018). Besides, the Ohmic contact is well preserved after Au NPs deposition and probe functionalization, indicating a reliable electrical contact for sensing test. There is a decrease on conductivity after Au NP sputtering, which is due to the impurity scattering effect on carriers.

The p-type semiconducting nature of MoS_2, as displayed in Fig. 2b, is resulted from oxygen incorporation, which is formed during the MoS_2 preparation process and exposure in ambient environment (Dolui et al., 2013). In theory, n-type semiconducting MoS_2 nanosheet is caused by sulfur vacancies in lattice. These vacancies can be occupied by oxygen (*i.e.*, acceptor impurity doping), and thus Fermi level shifts to the top of valence band, transferring the semiconductor to p-type. Meanwhile, the on/off ratio of these FET devices are around 3.6–3.8, which is in good agreement with previous studies on MoS_2 FETs with Si/SiO_2 substrate (Neal et al., 2017; Zhou et al., 2016). The decrease in slope of transfer curves within working region is found after AuNPs deposition. As studied in previous work (Chen et al., 2019), the carrier mobility (μ) is proportional to the slope, thus the declined slope suggests the decrease of carrier mobility, resulting from impurity scattering. There are no further changes on the output and transfer characteristics after probe functionalization. Since the aptamer probe is directly functionalized on AuNPs, they have no direct interaction and electrical interference to MoS_2. As for the I_{ds} in plateau region (*i.e.*, cut-off state current), it stands for the inverse saturation drain current, which is determined by minority carrier (*i.e.*, electron) density. The electron injection from MoS_2 to gold due to the work function difference causes the decrease of electron density in MoS_2, and as a result, the I_{ds} declines.

3.2. Sensor response and working mechanism

To study the response of MoS_2 sensor to KAN and verify the contribution of sensing probe, real-time I_{ds} responses were recorded while dropwise adding KAN solutions onto various platforms (*i.e.*, MoS_2, MoS_2/APT and MoS_2/APT/CS). At first, a bare electrode device (without MoS_2) was tested with KAN and there was no response observed (Fig. S3), which indicates that the direct conducting between gold electrodes via ion migration in aqueous solution does not generate sensing signal. As shown in Fig. 3a, the MoS_2 FET also shows negligible responses to KAN. This is because there is no specific interaction

between MoS_2 and KAN. Superior to graphene FET sensors showing responses to a wide variety of biomolecules due to delocalized π-bond induced chemically active surface, MoS_2 nanosheet shows no strong interaction with foreign analyte molecules. This also indicates that sensing probe is needed for the function of MoS_2 FET sensor. Further analysis was carried out by comparing the sensing signals of MoS_2/APT and MoS_2/APT/CS platforms. For MoS_2/APT platform, the current increases rapidly when KAN solution was added, which is due to the direct anchoring of KAN to APT. This interaction can form a more centralized structure compared with the single strand aptamer and leads to instaneous response, similar to previous study on aptamer/graphene FET sensor (Chen et al., 2019). The current increase in MoS_2/APT platform is caused by introducing more negative charges to p-type channel material surface (MoS_2 in this case). However, with MoS_2/APT/CS platform, KAN leads to a decreased current, and surprisingly, the current decrease continues for a period of time rather than an instant change after adding KAN (sharp current increase when adding KAN is from physical disturbance of injection). Therefore, a different sensing mechanism can be inferred on MoS_2/APT/CS platform, in which the interaction between probe and KAN is not instantaneous, slower than a direct APT-KAN bonding process. Based on current decrease, it is also suspected that the response of MoS_2/APT/CS is due to the reduce of negative charges on MoS_2 surface.

The electrical characteristic study on FET sensor could help to understand the sensing mechanism, thus transfer curves of MoS_2/APT/CS sensor were measured in KAN solutions at different concentrations. In Fig. 3b, the on/off ratio of MoS_2/APT/CS FET drops to 1.24–1.28, which is possibly because water media induces impurity scattering within MoS_2 plane and the variation in doping status of MoS_2 (Late et al., 2012). Transconductance (g_m) is the assessment of electronic transfer efficiency, defined as $\Delta I_{ds}/\Delta I_{gs}$, which is the slope of transfer curve within working region. It is obvious that g_m increases with KAN concentration increases. Since the value of g_m is proportional to carrier mobility, it can be inferred that KAN contributes to carrier mobility, that is, KAN helps to reduce the impurity scattering on channel material. While the scattering effect is known determined by doping level, KAN binding may also reduce the p-doping effect on MoS_2 channel. Furthermore, due to the electrostatic effect, the weaker p-doping could also be attributed to the decrease of negative charges on MoS_2 surface. Therefore, the introduction of KAN to APT/CS probe leads to a reduce of negative charges on MoS_2 surface, which is consistent with current responses shown in Fig. 3a. Increases in cut-off current ($I_{cut\text{-}off}$) is also observed in transfer curves when KAN concentration increases. As $I_{cut\text{-}off}$ is determined by the density of minority carriers, this trend indicates an increase of electron density (decrease of hole density), which is another evidence showing that KAN causes a loss of negative charges on MoS_2 surface.

To understand how KAN can induce surface charge state change of MoS_2, structure analysis on APT/CS probe and its reaction with KAN was performed. Fig. 4a displays the proposed reaction between KAN and APT/CS substance. The ssDNA aptamer 5′-TGG GGG TTG AGG CTA AGC CGA-3′ has been proved morphologically and chemically complementary with KAN, so that KAN can specifically bind to APT and form a chemically stable APT-KAN tertiary structure. The affinity between KAN and APT is strong enough to uncoil the base pairing of APT/CS and release CS chains (Robati et al., 2016). To confirm this, diphenylamine combined with UV detection (DPA-UV) was carried out on the sample solution after sensing test. DPA-UV method is a commonly-used chemical strategy to verify DNA. In theory, deoxyribose in DNA reacts with DPA indicator after heating in boiling water for 5 min, which produces a blue color chemical with a characteristic UV absorption peak at 595 nm (Jalkanen et al., 1980). The sensitivity of this test can be enhanced by adding a small amount of acetaldehyde. The DPA-UV results are presented in Fig. 4b. The inset optical image is the tested KAN solutions after interacting with DPA indicator. The solution tested on MoS_2/APT/CS platform shows light blue color while that on MoS_2/APT platform is colorless. In addition, an adsorption peak at 595 nm is found in UV absorption spectrum for solution tested on MoS_2/APT/CS platform and no peak shows in MoS_2/APT sample and pure buffer. The DPA-UV results confirm the release of CS DNA during KAN sensing with MoS_2/APT/CS platform, which is a direct evidence of replacement reaction between KAN and APT/CS.

Electrostatic effect and Debye screening effect are essential for chemical-electronic analysis with FET sensor. During the sensing process, CS is released into bulk solution, which induces the decrease of negative charges on MoS_2 surface. As shown in Fig. 4c, in DNA molecule, deoxynucleotides are linked by phosphodiester bonds to form a complete chain. The hydrolysis of deoxyribonucleotide will generate negative charges along DNA chains. Therefore, the release of negatively charged DNA chains induces charge state change of MoS_2. Electrostatic effect is critical for the sensing of FET device in aqueous media, but is limited by Debye screening effect (*i.e.*, Debye length) (Stern et al., 2007). Debye screening is based on electric double layer theory which suggests that a charged ion has electrostatic interaction with other ions in aqueous media, and the furthest effective distance of the charged ion can reach is Debye length (Vacic et al., 2011):

$$\lambda = \frac{1}{\sqrt{4\pi l_B \Sigma_i \rho_i z_i^2}}, \quad (1)$$

in which, l_B, ρ_i and z_i are Bjerrum length (0.7 nm), ion density and valence, respectively. In this study, the ion strength (defined as $\frac{1}{2}\Sigma_i \rho_i z_i^2$) of aqueous media is calculated by ion concentrations of PBS buffer (0.1 mM), and Debye length is determined to be 5.88 nm. Considering the height profile shown in the AFM measurement (Fig. 1i), the probe height shows an average level of 5.66 nm. Therefore, all charges on APT and CS can electrically influence the carrier distribution on MoS_2 surface. To facilitate understanding, the schematic of charges on probe is illustrated in Fig. 4d. The addition of KAN uncoils APT/CS pairing and forms a complex APT/KAN by specific non-covalent interactions. The reduced negative charges within the Debye length from MoS_2 surface after the replacement of CS by KAN could reduce the p-doping on MoS_2 surface. Thus, the decrease of hole density in MoS_2 plays the major role in current drop during KAN introduction. Moreover, since the APT-CS uncoiling, APT-KAN refolding and CS release processes proceed along the time and cannot be finished instantaneously, thus the drain current shows a continuous decline after adding KAN solutions.

Compared with MoS_2/APT platform based on direct binding of KAN with APT, MoS_2/APT/CS platform has superiority in sensing reliability with decreased device-to-device variations. KAN sensing tests were carried out on three sensor devices of each type at concentrations from 10^{-9} M to 10^{-4} M. Based on sensing results (Fig. S5), it is found that the data points from MoS_2/APT/CS platform at each concentration are more centralized than those from MoS_2/APT platform, indicating smaller device-to-device variations. The minimized device-to-device variations are related to probe design and KAN sensing mechanism. In contrast to regulated configuration of APT paired with CS, the morphology of APT alone shows wide possibilities since APT is a single strand DNA and each ssDNA may exhibit different degree of folding induced by free bending. The CS constrains and stabilizes the shape of APT by pairing bases along both ends of aptamer. Thus, CS-regulated APT shows smaller variations in KAN binding process. The enhancement in sensing reliability with decreased device-to-device variations will contribute to applicability of FET sensors in practical applications.

3.3. Antibiotic sensing capability

To quantitatively study the detection capability and sensitivity of MoS_2/APT/CS sensors for KAN, concentration-dependent tests were carried out. To make a direct comparison, current responses are normalized by the initial current in DI water. Time-resolved response curves for KAN solutions from 0 M to 10^{-4} M are presented in Fig. 5a.

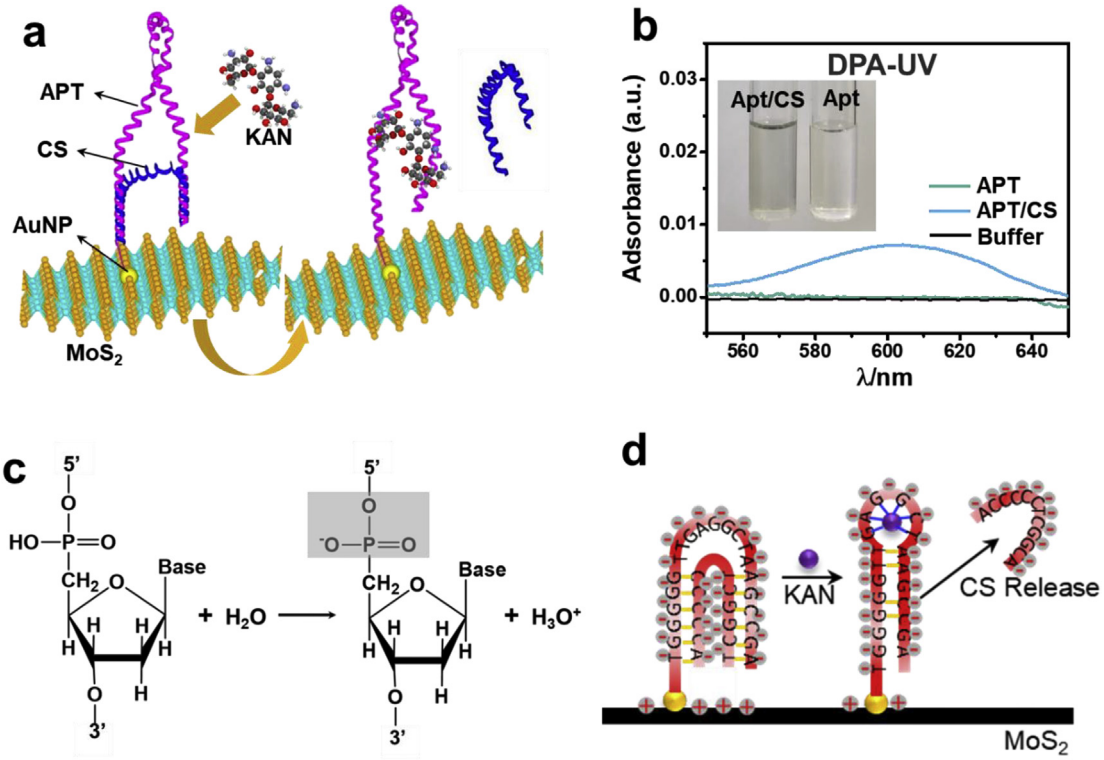

Fig. 4. (a) Schematic diagram of structure and substance change on MoS2/APT/CS platform after introduction of KAN. (b) Diphenylamine method and UV absorption spectra of pure buffer and samples collected after sensing test on MoS2/APT and MoS2/APT/CS platforms. Inset is the optical picture of samples collected after sensing test. (c) Hydrolysis of deoxyribonucleotide: the origin of negative charge along DNA chains. (d) KAN sensing principle with MoS2/APT/CS platform through a replacement reaction.

Sensors show decreased current after adding KAN and the current decreasing slope in initial reaction period increases with KAN concentration. This indicates increased reaction rates at higher concentrations of KAN. Besides, there is a maximum response level found for higher concentrations (e.g., 10^{-4} M, 10^{-5} M, 10^{-6} M), which is due to the saturation of binding sites on the probe. From the prospective of chemical equilibrium theory, the interaction is described as:

$$\text{APT/CS} + \text{KAN} = \text{APT/KAN} + \text{CS (k)}, \quad (2)$$

where k is the reaction rate constant of replacement reaction. From chemical reaction theory, the reaction rate (r) can be given by:

$$r = -\frac{d[\text{APT/CS}]}{dt} = k\,[\text{APT/CS}]\,[\text{KAN}], \quad (3)$$

in which the *[APT/CS]* and *[KAN]* are the concentration of APT/CS and KAN, respectively. Since *[APT/CS]* level is determined once the sensor is prepared and thus the reaction rate (*d[APT/CS]/dt*) has a positive correlation with KAN concentration. Therefore, this could explain the response time difference when sensing KAN at varying concentrations.

To further study the sensing performance based on interaction kinetics, the relative response of each concentration at t = 20 s, 70 s, 130 s and 300 s (sample solutions were introduced at t = 0 s) were calculated from parallel experiments on six similar MoS_2/APT/CS sensors. Relative responses were calculated by $(I_0–I)/I_0$, in which I_0 is the sensor current in pure buffer with no KAN and I is the current after

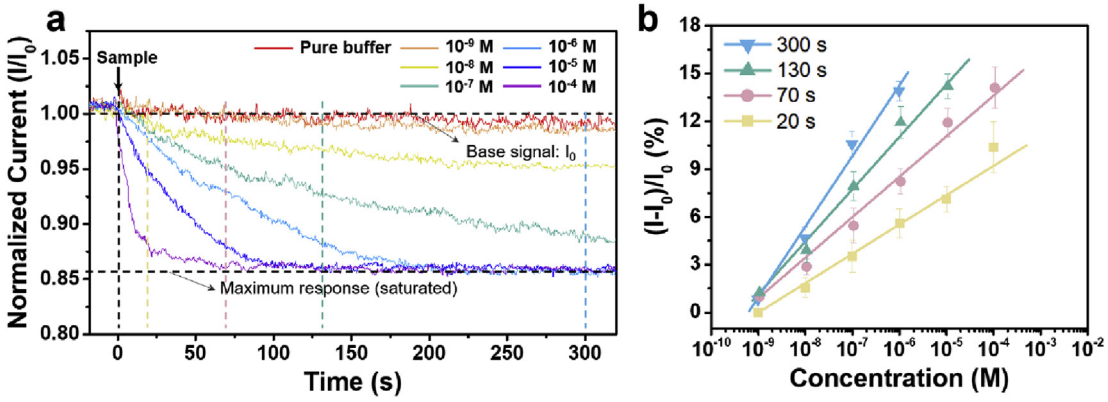

Fig. 5. (a) Time-resolved normalized current responses of KAN at concentrations from 10-9 M to 10-4 M. KAN solutions are introduced onto sensing platform after forming a stable base current in DI water. Normalized current is obtained by the ratio of response current vs. base current. (b) Relative response vs. KAN concentration (in logarithmic coordinate) at t = 20 s, t = 70 s, t = 130 s, and t = 300 s. The relative response is calculated by (I–I0)/I0. Error bars are obtained based on six parallel experiments.

adding KAN, respectively. At different sensing times, the relative response vs. logarithmic KAN concentration shows linear correlations within different concentration ranges, as plotted in Fig. 5b. The sensor sensitivity is defined by the sensor relative response ($(I_0–I)/I_0$) per unit KAN concentration (C), which can be determined by the slope of fitted line. Therefore, our sensor shows increasing sensitivity by prolonging detection time. The sensitivity at 20 s, 70 s, 130 s and 300 s were calculated as 1.85 M^{-1}, 2.55 M^{-1}, 3.35 M^{-1} and 4.43 M^{-1}, respectively. In addition, for different sensing time, the linear working range is different. A longer sensing time results in a narrower linear working range. For example, the linear working ranges for t = 20 s and 300 s are 10^{-9}-10^{-4} M and 10^{-9}-10^{-6} M, respectively. This can be ascribed to the quick saturation of current signal at high KAN concentrations.

LOD is an important parameter to evaluate sensor capability. It is calculated by applying the value of minimum response signal into the fitting equation of normalized drain current *vs.* KAN concentration. Since the maximum noise level is determined to be 0.5% as the maximum deviation of normalized drain current from its average level, and the signal-to-noise ratio is 3 defined from previous studies (Li et al., 2012, 2013), the reliable minimum sensing signal is determined to be 1.5%. With the fitting equations of sensing signal and KAN concentration shown in **Text S1**, the LODs of MoS_2/APT/CS sensor for KAN are calculated to be 1.06 nM (20 s), 1.04 nM (70 s), 0.79 nM (130 s) and 0.66 nM (300 s), respectively. The LOD values of our sensor are comparable to antibiotic residues in water body (nM level), indicating a practical sensing promise for antibiotic monitoring in water. As KAN and ATP show a replacement reaction feature, the sensing time plays important role in tuning the sensor sensitivity, LOD and linear working range.

3.4. Sensor specificity

Specificity is critical and becomes a bottleneck for the real applications of antibiotic FET sensor. To determine the specificity of MoS_2/APT/CS sensor, sensing tests and quantitative comparison were carried out with other five antibiotics of four categories. Streptomycin (STR) and tobramycin (TOB) are another two aminoglycosides with similar functional groups as KAN. Amoxicillin (AMX) has the highest detection rate and concentration in surface water as a beta-lactam. Ciprofloxacin (CIP) is one of the most widely used antibiotics from quinolones because of its broad-spectrum property, and chloramphenicol (CHL) has hematologic toxicity and is long-standing in water due to its chemical stability. Fig. S6 shows sensor responses towards five mismatched antibiotics with concentration from 10^{-9} M to 10^{-4} M. There is no significant response observed for these antibiotics. To quantify response variations and verify sensor selectivity, sensing tests were repeated on six to ten similar sensors and their sensitivities for each antibiotic at various concentrations were plotted in Fig. 6a. The average values of relative responses for other five antibiotics range from −0.9% to 1.3% with a maximum value of 1.87%, which is much lower than that of KAN (14.8% at 10^{-4} M). The results indicate that MoS_2/APT/CS platform shows insignificant responses to mismatched antibiotics. Here we use “selectivity coefficient” to quantitatively analyze selectivity. It is defined as the ratio of the response of target analyte (KAN) to that of interfering chemical (mismatched antibiotic) at the same concentration. For comparison, selectivity coefficients of representative antibiotic sensors are listed in Table S1. It is shown that the selectivity coefficient (12.8) of MoS_2/APT/CS sensor is much higher than those of reported antibiotic sensing platforms, confirming the superior selectivity of this sensor over others.

In real water monitoring, various antibiotics coexist; therefore, sensing tests with mixed antibiotics were carried out. One control test was performed with continuous adding of different antibiotics and another test was performed by adding antibiotic mixtures without and with KAN. As shown in Fig. 6b, MoS_2/APT/CS platform shows no significant responses to mismatched antibiotics; while big current decreases can be observed when adding KAN alone and antibiotic mixture with KAN. These results indicate a high specificity of this sensor in complex water body analysis with coexist antibiotics. Currently, the MoS_2/APT/CS sensor is one-time use. Through dissociation of KAN and APT complex with chemical treatment (e.g., use sodium dodecyl sulfate solution) (Wang et al., 2017b), the sensor may work for multiple times.

3.5. Real water sample test

The practical feasibility of this sensor for KAN detection in real water was studied through a recovery assay. Tap water and Taihu Lake water (Wuxi, China) were collected as real water samples, preprocessed by filtering before being used. In recovery tests, different doses of KAN were accurately added into the water samples and the obtained sample solutions with different concentrations of KAN were tested with MoS_2/APT/CS sensing platform. Drain current response signals at t = 20 s were analyzed combined with the standard fitting curve. The measured KAN concentrations of each sample were summarized in Table S2. The recoveries were obtained from three groups of parallel tests (n = 6) for each. The recoveries are 107.5% and 94.5% in tap water with KAN concentrations of 0.2 μM and 1.0 μM, while those for Taihu Lake water were 113.5% and 109.6%. The inferior recovery in Taihu Lake water to that of tap water can be attributed to the more complex water media, in which some chemicals may pose interference on the sensing signal. The results of recovery tests in real water samples demonstrate the potential feasibility of this sensor platform for practical applications of antibiotic sensing.

4. Conclusions

In summary, we report a new sensor structure for label-free detection of kanamycin on MoS_2 field-effect transistor, in which the aptamer DNA probe is shaped by a short complementary strand. We experimentally demonstrate that the sensor platform achieves an ultratrace antibiotic detection capability with an LOD of 0.66 nM–1.06 nM, a sensing time-dependent sensitivity and linear working range, as well as an extremely high selectivity against other antibiotics. The advanced probe geometry also contributes to an improved reliability of the sensor compared with single-component probe for decreased device-to-device variations. A new sensing mechanism based on a replacement reaction is proposed through an in-depth understanding of FET electronics and interface-solution chemistry. The sensor working principle relies on charge release from probe, which overcomes Debye screening limitation and enhances the selective detection. Meanwhile, for practical and commercial applications, further optimizations are required on this sensor, including modification on bare MoS_2 surface for enhanced chemical stability and a shield from non-specific interactions with detecting media, as well as an effective strategy for channel material deposition for large-scale and uniform fabrication. We believe this study will promote FET sensing platform both in theory and in experimental demonstration, potentially open a broader research scope from antibiotics detection to chemical and biological sensing.

CRediT authorship contribution statement

Xiaoyan Chen: Conceptualization, Data curation, Formal analysis, Investigation, Methodology, Validation, Writing - original draft. **Sibei Hao:** Data curation, Formal analysis, Investigation, Methodology. **Boyang Zong:** Data curation, Formal analysis, Investigation, Methodology. **Chengbin Liu:** Data curation, Formal analysis, Investigation, Methodology. **Shun Mao:** Conceptualization, Funding acquisition, Project administration, Resources, Software, Supervision, Validation, Writing - review & editing.

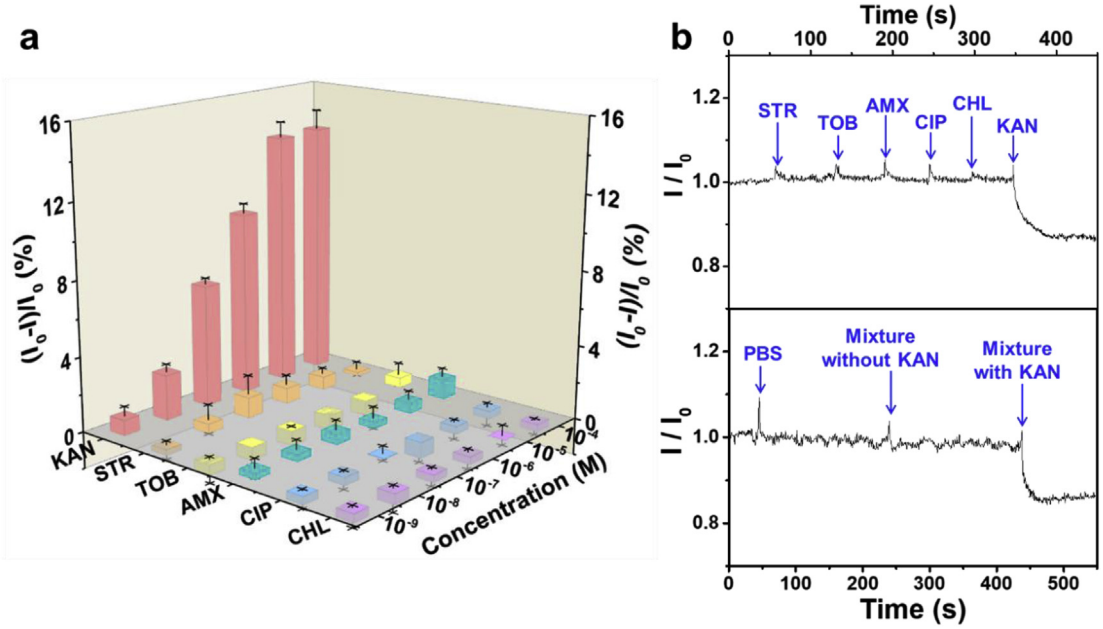

Fig. 6. (a) Responses of MoS2/APT/CS sensor to six antibiotics (i.e., STR, TOB, AMX, CIP, CHL and KAN) at concentrations from 10-9 M to 10-4 M. (b) Real-time sensor responses by continuous adding different antibiotics and antibiotic mixtures without and with KAN. Concentrations of all antibiotics are 10–4 M.

Declaration of competing interest

The authors declare that they have no known competing financial interests or personal relationships that could have appeared to influence the work reported in this paper.

Acknowledgements

This work was supported by the National Natural Science Foundation of China (No. 21707102) and the Fundamental Research Funds for the Central Universities, China (No. 22120180524).

Appendix A. Supplementary data

Supplementary data to this article can be found online at https://doi.org/10.1016/j.bios.2019.111711.

References

Bayen, S., Yi, X., Segovia, E., Zhou, Z., Kelly, B.C., 2014. J. Chromatogr. A 1338, 38–43.
Boxall, A.B.A., Rudd, M.A., Brooks, B.W., Caldwell, D.J., Choi, K., Hickmann, S., Innes, E., Ostapyk, K., Staveley, J.P., Verslycke, T., Ankley, G.T., Beazley, K.F., Belanger, S.E., Berninger, J.P., Carriquiriborde, P., Coors, A., DeLeo, P.C., Dyer, S.D., Ericson, J.F., Gagné, F., Giesy, J.P., Gouin, T., Hallstrom, L., Karlsson, M.V., Larsson, D.G.J., Lazorchak, J.M., Mastrocco, F., McLaughlin, A., McMaster, M.E., Meyerhoff, R.D., Moore, R., Parrott, J.L., Snape, J.R., Murray-Smith, R., Servos, M.R., Sibley, P.K., Straub, J.O., Szabo, N.D., Topp, E., Tetreault, G.R., Trudeau, V.L., Kraak, G.V.D., 2012. Environ. Health Perspect. 120 (9), 1221–1229.
Chen, X., Liu, Y., Fang, X., Li, Z., Pu, H., Chang, J., Chen, J., Mao, S., 2019. Biosens. Bioelectron. 126, 664–671.
Chuang, H.-J., Chamlagain, B., Koehler, M., Perera, M.M., Yan, J., Mandrus, D., Tománek, D., Zhou, Z., 2016. Nano Lett. 16 (3), 1896–1902.
Darmostuk, M., Rimpelova, S., Gbelcova, H., Ruml, T., 2015. Biotechnol. Adv. 33 (6), 1141–1161 Part 2.
Dolui, K., Rungger, I., Sanvito, S., 2013. Phys. Rev. B 87 (16), 165402.
Fang, X., Chen, X., Liu, Y., Li, Q., Zeng, Z., Maiyalagan, T., Mao, S., 2019. ACS Appl. Nano Mater. 2 (4), 2367–2376.
Fu, W., Jiang, L., van Geest, E.P., Lima, L.M., Schneider, G.F., 2017. Adv. Mater. 29, 1603610.
Fuhrer, M.S., Hone, J., 2013. Nat. Nanotechnol. 8, 146.
Island, J.O., Steele, G.A., Zant, H.S.J.v.d., Castellanos-Gomez, A., 2015. 2D Mater. 2 (1), 011002.
Jalkanen, M., Larjava, H., Turakainen, H., Tammi, M., 1980. J. Biochem. Biophys. Methods 3 (4), 195–199.
Knecht, B.G., Strasser, A., Dietrich, R., Märtlbauer, E., Niessner, R., Weller, M.G., 2004. Anal. Chem. 76 (3), 646–654.
Knopfmacher, O., Hammock, M.L., Appleton, A.L., Schwartz, G., Mei, J., Lei, T., Pei, J., Bao, Z., 2014. Nat. Commun. 5, 2954.
Kumar, K., Thompson, A., Singh, A.K., Chander, Y., Gupta, S.C., 2004. J. Environ. Qual. 33 (1), 250–256.
Late, D.J., Liu, B., Matte, H.S.S.R., Dravid, V.P., Rao, C.N.R., 2012. ACS Nano 6 (6), 5635–5641.
Lee, C., Yan, H., Brus, L.E., Heinz, T.F., Hone, J., Ryu, S., 2010. ACS Nano 4 (5), 2695–2700.
Li, H., Yin, Z., He, Q., Li, H., Huang, X., Lu, G., Fam, D.W.H., Tok, A.I.Y., Zhang, Q., Zhang, H., 2012. Small 8 (1), 63–67.
Li, H., Shi, W., Song, J., Jang, H.-J., Dailey, J., Yu, J., Katz, H.E., 2019. Chem. Rev. 119 (1), 3–35.
Li, M., Zhou, X., Guo, S., Wu, N., 2013. Biosens. Bioelectron. 43, 69–74.
Majd, S.M., Salimi, A., Ghasemi, F., 2018. Biosens. Bioelectron. 105, 6–13.
Mao, S., Chang, J., Pu, H., Lu, G., He, Q., Zhang, H., Chen, J., 2017. Chem. Soc. Rev. 46 (22), 6872–6904.
Meric, I., Han, M.Y., Young, A.F., Ozyilmaz, B., Kim, P., Shepard, K.L., 2008. Nat. Nanotechnol. 3, 654.
Min, K.-A., Park, J., Wallace, R.M., Cho, K., Hong, S., 2016. 2D Mater. 4 (1), 015019.
Nakatsuka, N., Yang, K.-A., Abendroth, J.M., Cheung, K.M., Xu, X., Yang, H., Zhao, C., Zhu, B., Rim, Y.S., Yang, Y., Weiss, P.S., Stojanović, M.N., Andrews, A.M., 2018. Science 362 (6412), 319–324.
Neal, A.T., Pachter, R., Mou, S., 2017. Appl. Phys. Lett. 110 (19), 193103.
Radisavljevic, B., Radenovic, A., Brivio, J., Giacometti, V., Kis, A., 2011. Nat. Nanotechnol. 6, 147.
Radisavljevic, B., Kis, A., 2013. Nat. Nanotechnol. 8, 147.
Robati, R.Y., Arab, A., Ramezani, M., Langroodi, F.A., Abnous, K., Taghdisi, S.M., 2016. Biosens. Bioelectron. 82, 162–172.
Stern, E., Wagner, R., Sigworth, F.J., Breaker, R., Fahmy, T.M., Reed, M.A., 2007. Nano Lett. 7 (11), 3405–3409.
Tlili, I., Caria, G., Ouddane, B., Ghorbel-Abid, I., Ternane, R., Trabelsi-Ayadi, M., Net, S., 2016. Sci. Total Environ. 563–564, 424–433.
Turiel, E., Bordin, G., Rodríguez, A.R., 2003. J. Chromatogr. A 1008 (2), 145–155.
Vacic, A., Criscione, J.M., Rajan, N.K., Stern, E., Fahmy, T.M., Reed, M.A., 2011. J. Am. Chem. Soc. 133 (35), 13886–13889.
Vicarelli, L., Vitiello, M.S., Coquillat, D., Lombardo, A., Ferrari, A.C., Knap, W., Polini, M., Pellegrini, V., Tredicucci, A., 2012. Nat. Mater. 11, 865.
Wang, C., Li, Y., Zhu, Y., Zhou, X., Lin, Q., He, M., 2016. Adv. Funct. Mater. 26 (42), 7668–7678.
Wang, J.-W., Liu, Y.-P., Chen, P.-H., Chuang, M.-H., Pezeshki, A., Ling, D.-C., Chen, J.-C., Chen, Y.-F., Lee, Y.-H., 2018. Adv. Electron. Mater. 4 (1), 1700340.
Wang, L., Wang, Y., Wong, J.I., Palacios, T., Kong, J., Yang, H.Y., 2014. Small 10 (6), 1101–1105.
Wang, Q.H., Kalantar-Zadeh, K., Kis, A., Coleman, J.N., Strano, M.S., 2012. Nat. Nanotechnol. 7, 699.
Wang, R., Zhou, X., Liedberg, B., Zhu, X., Memon, A.G., Shi, H., 2017a. ACS Appl. Mater. Interfaces 9 (40), 35492–35497.
Wang, R., Zhou, X., Zhu, X., Yang, C., Liu, L., Shi, H., 2017b. ACS Sens. 2 (2), 257–262.
Zhang, C., Chen, P., Hu, W., 2015. Chem. Soc. Rev. 44 (8), 2087–2107.
Zhao, M., Zhuo, Y., Chai, Y.-Q., Yuan, R., 2015. Biomaterials 52, 476–483.
Zhou, G., Chang, J., Pu, H., Shi, K., Mao, S., Sui, X., Ren, R., Cui, S., Chen, J., 2016. ACS Sens. 1 (3), 295–302.